

Emergent Antiferromagnetic Behavior in EuCl_3 Monolayer: A Comprehensive First-Principles Study Including Hubbard-SOC Interplay

Nurcan Kutluk Kalkan,¹ Ilkay Ozdemir,^{1,2} Yusuf Yüksel,³ Ümit Akıncı,³ Johannes V. Barth,⁴ and Ethem Aktürk^{1,4,*}

¹*Physics Department, Adnan Menderes University, 09100 Aydın, Turkey*

²*Department of Physics, University of Antwerp, Groenenborgerlaan 171, B-2020 Antwerp, Belgium*

³*Physics Department, Faculty of Science, Tinaztepe Campus, Dokuz Eylül University, 35390 İzmir, Turkey.*

⁴*Physics Department E20, Technical University of Munich (TUM),*

James Franck Strasse1, 85748, Garching (Germany)

(Dated: December 11, 2023)

We present a comprehensive study on the electronic and magnetic properties of the EuCl_3 monolayer using first-principles calculations. By taking into account the spin-orbit coupling (SOC) and the Hubbard effects, we elucidate the influence of these interactions on the structural properties of EuCl_3 monolayer. Comparing the lattice parameters obtained with the PBE+SOC and PBE+SOC+Hubbard effects reveals an increase in the lattice parameters when including the Hubbard effect. In the absence of the Hubbard interaction, the magnetic ground state of the EuCl_3 monolayer exhibits a preference for a ferromagnetic (FM) configuration as determined by the PBE+SOC calculations. However, the introduction of the Hubbard parameter leads to a shift in the magnetic ground state preference towards an antiferromagnetic (AFM) Néel state. Based on the calculated energy values, Monte Carlo simulations are carried out to determine the Néel temperature (T_N). Our simulations yield a Néel temperature of 390 K for the EuCl_3 monolayer, indicating the temperature at which the transition from a paramagnetic phase to an antiferromagnetic phase occurs. These results highlight the importance of incorporating the SOC and the Hubbard effect in accurately describing the electronic and magnetic properties of the EuCl_3 monolayer. Our results contribute to a deeper understanding of the fundamental physics underlying the behavior of this intriguing two-dimensional material and provide insights into its potential applications in spintronics and magnetic devices.

I. INTRODUCTION

Spintronics research has experienced significant growth recently, particularly in the exploration of two-dimensional (2D) van der Waals (vdW) structures¹⁻⁵. These structures have emerged as a prominent area of investigation, enabling fundamental studies of spin-based devices and facilitating various spin injection and spin-polarized transport theories⁶. 2D vdW magnets exhibit intrinsic ferromagnetic (FM) and antiferromagnetic (AFM) ground states, even at atomic layer thicknesses, thus presenting exciting opportunities for materials science and the development of spin-related applications. The layered structure of these 2D vdW magnetic systems offers advantages such as atomic layer divisibility and magnetic anisotropy, effectively suppressing spin fluctuations⁷. Consequently, they provide an ideal platform for both theoretical and experimental exploration of phase transitions at the 2D boundary. Despite these advancements, two major challenges persist in the realm of 2D structures. Firstly, the identification of materials that demonstrate stability under ambient conditions, possess long-term operational suitability, and exhibit sufficient mechanical strength remains essential⁸. Secondly, it is crucial to elevate the magnetic phase transition temperatures above room temperature. Among the significant properties of magnetic materials, the critical temperature (T_c) holds paramount importance as it represents the temperature at which magnetic order is lost. Achieving a high T_c , surpassing room temperature, becomes a critical requirement for effective implementation of FM spintronic devices⁷.

The Mermin-Wagner theorem first established constraints on the presence of long-range magnetic order in 2D systems at finite temperature⁹. According to this theorem, the spontaneous breaking of continuous symmetries, such as the rotational symmetry or the U(1) spin symmetry, is prohibited in 2D systems at any finite temperature. This would suggest an absence of long-range magnetic order in 2D materials. However, the conventional understanding was challenged in 2017 with the discovery of ferromagnetism in monolayer CrI₃¹⁰. Key to understanding this apparent contradiction is the interplay of several factors, including the inherent magnetic anisotropy due to the strong spin-orbit coupling and the role of defects or lattice distortions. Following this experimental discovery, demonstrating the ability of a 2D material to maintain magnetization at a non-zero temperature, 2D magnetic materials have been at the forefront of both theoretical¹¹⁻¹³ and experimental¹⁴⁻¹⁶ scientific investigations. In the case of the CrI₃ monolayer, the ferromagnetism appears to arise from a combination of robust magnetic anisotropy and the suppression of thermal fluctuations due to quantum confinement¹⁰. The existence of an out-of-plane easy-axis magnetic anisotropy in CrI₃, originating from interlayer magnetic coupling, helps stabilize the ferromagnetic order in the monolayer despite the limitations imposed by the Mermin-Wagner theorem. Further studies, both experimental and theoretical, have also unveiled the presence of magnetism when other chalcogen atoms are incorporated. For instance, bulk CrBr₃ is an easy-axis ferromagnet with a Curie temperature (T_c) of 33 K¹⁷, and it retains ferromagnetism even at monolayer thickness, exhibiting pronounced out-of-plane anisotropy^{18,19}. Conversely, bulk CrCl₃ is an easy-plane A-type antiferromagnet¹⁷, while investigations on few-layer samples have highlighted an enhancement of the antiferromagnetic interlayer exchange compared to bulk crystals^{20,21}.

On the other hand, rare-earth metal elements, especially gadolinium (Gd) and europium (Eu), possess half-filled and highly localized 4f subshells, leading to large magnetic moments and strong spin-orbit coupling (SOC) compared to transition metal elements^{22,23}. As a result, due to their unique electronic and magnetic properties, rare-earth-based 2D materials, especially monolayers composed of Gd or Eu, have garnered increasing attention. These materials provide an exciting platform for investigating novel phenomena and advancing technologies such as spintronics, quantum computing, and magnetic storage devices. Gd-based monolayers, renowned for their high Curie temperatures near room temperature, exhibit robust magnetic properties, positioning them as promising candidates for spintronic applications²⁴⁻²⁶. Moreover, it has been reported that Eu doping in two-dimensional materials can enhance their electronic properties, magnetism, and critical temperature²⁷⁻³¹. Building upon these findings, our study focuses on investigating the electronic and magnetic properties of the EuCl₃ monolayer. Our calculations incorporated the Hubbard effect along with SOC to better define the structure, considering previous studies that have highlighted the significance of this addition³²⁻³⁷. Comparison of lattice parameters obtained under the PBE+SOC and PBE+SOC+Hubbard effects revealed that the inclusion of the Hubbard effect led to an increase in lattice parameters. While the magnetic ground state of EuCl₃ favored a ferromagnetic (FM) configuration in the PBE+SOC calculations, the introduction of Hubbard parameter shifted the preference to an antiferromagnetic (AFM) Néel state. Magnetic anisotropy energies were obtained by exploring different spin orientations within the structure. Based on the resulting energy values, Monte Carlo simulations were performed, determining a Néel temperature (T_N) of 390 K for EuCl₃ monolayer.

II. COMPUTATIONAL METHODS

First-principles calculations were carried out using the spin-polarized density functional theory (DFT) implemented in the Vienna Ab initio Simulation Package (VASP)^{38,39}. We described the ion-electron interactions by using projector augmented wave (PAW) potentials^{40,41}. The Perdew-Burke-Ernzerhof (PBE) functional⁴², which is based on the

generalized gradient approximation (GGA), was employed to account for the exchange-correlation interactions. The electronic and magnetic properties of the system were determined by solving the Kohn-Sham equations self-consistently within this framework. The calculations were performed with a finite basis set using plane-wave expansions, and a cutoff energy of 340 eV was chosen to ensure convergence. To account for the van der Waals interactions, the DFT-D2 correction⁴³ scheme was included. The Brillouin zone integration was performed using a $12 \times 12 \times 1$ mesh points in \mathbf{k} -space within Monkhorst-Pack grid⁴⁴. To optimize the atomic positions and lattice constants, we employed the conjugate-gradient algorithm^{45,46}. The optimization process involved minimizing the total energy and forces to ensure convergence. A convergence criterion of 10^{-5} eV was set, ensuring that the energy difference between two consecutive steps reached a sufficiently low value. During the ionic relaxation, the maximum Hellmann-Feynman forces acting on each atom were constrained to be below $0.01 \text{ eV}/\text{\AA}$, guaranteeing stability within the system. Moreover, the maximum pressure exerted on the unit cell was maintained below 1 kbar. To handle the electronic occupations, we implemented the Gaussian-type Fermi-level smearing method with a smearing width of 0.01 eV. Visualization of the structures was achieved using the VESTA program⁴⁷.

All calculations, unless otherwise stated, incorporated the effects of spin-orbit coupling (SOC) and Hubbard interactions. The inclusion of SOC accounts for the strong interaction between the electron spin and its orbital motion, which is crucial for accurately describing the electronic and magnetic properties of the system. Additionally, the Hubbard effect, accounting for the on-site electron-electron interactions, was considered to better capture the electronic correlations within the system. To determine the appropriate effective Coulomb interaction parameter (U_{eff}) for the EuCl_3 monolayer, the linear response approach introduced by Cococcioni and De Gironcoli⁴⁸ was employed by using the VASP program. Specifically, the effective U value for the EuCl_3 monolayer was found to be $U_{eff}=8.9 \text{ eV}$. (See the Supporting Information⁴⁹ for more details.) Our obtained value is comparable with the findings from Pradip et al.⁵⁰, who investigated the EuO crystal structure. In their study, they determined the U value for the f -orbitals of Eu as 8.3 eV and the J value as 0.77 eV. By incorporating SOC and the Hubbard effect, our calculations provide a comprehensive understanding of the electronic and magnetic properties of the EuCl_3 monolayer.

We calculated the work function W for the EuCl_3 monolayer by the difference⁵¹

$$W = -e\phi - E_F \quad (1)$$

where $-e$ represents the charge of an electron, ϕ denotes the electrostatic potential in the vacuum nearby the surface, and E_F is the Fermi level, which corresponds to the electrochemical potential of electrons within the material. The term $-e\phi$ represents the energy of a stationary electron in the vacuum nearby the surface.

To investigate the magnetic properties of the EuCl_3 monolayer, we employed an atomistic spin Hamiltonian based on a classical Heisenberg model, which can be expressed by the following equation:

$$\begin{aligned} \mathcal{H} = & -J_1 \sum_{\langle ij \rangle_1} \vec{\mu}_i \cdot \vec{\mu}_j - J_2 \sum_{\langle ik \rangle_2} \vec{\mu}_i \cdot \vec{\mu}_k - J_3 \sum_{\langle il \rangle_3} \vec{\mu}_i \cdot \vec{\mu}_l \\ & - \sum_i (k_x \mu_{ix}^2 + k_y \mu_{iy}^2 + k_z \mu_{iz}^2), \end{aligned} \quad (2)$$

Here, $\vec{\mu}_i$ represents the classical magnetic dipole moment located at site i within a honeycomb lattice of linear dimension $L = 100$. J_1 , J_2 , and J_3 denote the exchange coupling between nearest, second-nearest, and third-nearest neighbor spins, respectively. We considered four distinct magnetic configurations, comprising one ferromagnetic state and three antiferromagnetic states. These magnetic configurations are illustrated in Fig. 2. To determine the values of the exchange coupling parameters, we calculated the total energies associated with each magnetic configuration and employed these calculated energies in the equations provided in the Supporting Information⁴⁹. The fourth term in Equation 2 accounts for the contribution of single-ion anisotropy to the total energy per spin.

In order to delve deeper into the magnetic properties of the EuCl_3 monolayer, we carried out Monte Carlo simulations in addition to the DFT calculations. By combining these two computational techniques, we aimed to provide a comprehensive understanding of the magnetic behavior in EuCl_3 monolayer. The Monte Carlo simulations were based on the microscopic Hamiltonian, treating each spin as a classical vector with a magnitude of $|\vec{\mu}| = 6.0 \mu_B$. The simulations utilized the Metropolis update scheme^{52,53} and incorporated periodic boundary conditions in each direction. To minimize statistical errors, we considered 50 different sample realizations at each temperature. Starting from a randomly oriented initial configuration at a temperature well above the critical temperature of the system, we gradually decreased the temperature in small steps while monitoring various thermal and magnetic properties, including the magnetic order parameter $\mathbf{O} = \frac{1}{L^2} \sum_{i=1}^{L^2} (-1)^i \vec{\mu}_i$ and the heat capacity $\mathbf{C} = \partial \langle \mathcal{H} \rangle / \partial T$.

III. RESULTS

EuCl₃ monolayer, examined in this study, exhibits a trigonal symmetry within the $P\bar{3}1m$ space group, similar to the well-known transition metal trihalides³⁶. Its optimized crystal structure, as shown in Fig. 1, comprises a single layer of europium (Eu) atoms situated between two layers of chlorine (Cl) atoms. Within this crystal structure, each Eu atom is coordinated by six Cl atoms, resulting in an octahedral coordination geometry. The Eu atoms are arranged in a honeycomb lattice, with three neighboring Cl atoms bonded to each Eu atom from opposing sides. The Cl atoms form hexagonal layers positioned above and below the Eu layer, thus creating a structure with three-atomic-layer.

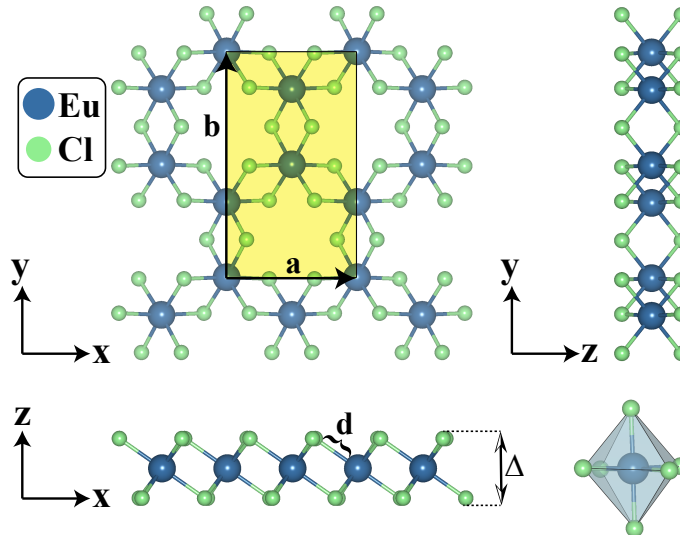


Figure 1. Crystal structure of the EuCl₃ monolayer, presented from three different views. The unit cell is highlighted with a yellow shaded area. The octahedral geometry is also given inset, which is depicted in blue shading.

In the first step, we performed the optimization of the EuCl₃ monolayer using the standard PBE method, which provided a baseline structure. Subsequently, to take into account for the spin-orbit coupling (SOC) effect, we incorporated it into the calculation and further optimized the structure using the PBE+SOC method. Finally, we enhanced the accuracy of our study by introducing the Hubbard effect, which considers the localized electrons in the f -orbitals of the Eu atom. This comprehensive approach, known as PBE+SOC+U calculation, enables a more thorough treatment of electronic interactions. In the latter case, we observed an expansion of the lattice parameters, in particular a 2% increase in the x -crystallographic direction and a 0.1% increase in the y -crystallographic direction. The calculated structural parameters are presented together in Table I.

Table I. Structural parameters of the EuCl₃ monolayer calculated using different methods (PBE, PBE+SOC, PBE+SOC+U): Lattice constants along the x -crystallographic direction ($|\vec{a}|=a$) and the y -crystallographic direction ($|\vec{b}|=b$); thickness parameter (Δ); average bond lengths between neighboring Eu and Cl atoms (d); and average magnetic moment on the unit cell (μ).

| method | a (Å) | b (Å) | Δ (Å) | d (Å) | μ (μ_B) |
|-----------|-------|-------|--------------|-------|-------------------|
| PBE | 6.64 | 11.77 | 3.11 | 2.70 | 24.00 |
| PBE+SOC | 6.64 | 11.77 | 3.11 | 2.70 | 23.86 |
| PBE+SOC+U | 6.77 | 11.79 | 3.06 | 2.69 | 23.79 |

After performing the structural optimization, we proceeded to analyze the ground state of the EuCl₃ monolayer in terms of magnetism. In order to determine the most favorable magnetic ground state configuration, we examined four different spin configurations for the europium atoms, as depicted in Fig. 2. These configurations are labeled as ferromagnetic (FM), antiferromagnetic-Néel (AFM-Néel), AFM-Stripy, and AFM-Zigzag. Our results from the PBE+SOC calculations indicated that the EuCl₃ monolayer prefers a ferromagnetic configuration as its magnetic ground state. However, upon incorporating the Hubbard effect through PBE+SOC+U calculations, the magnetic ground state preference shifted to an antiferromagnetic Néel state. We provided the relative energies of magnetic

configurations with respect to the corresponding minimum energy configurations, both calculated without and with the inclusion of the Hubbard parameter, in the Supporting Information⁴⁹. The inclusion of the Hubbard term provides a more accurate treatment of the electron-electron interactions, particularly those involving the localized f -orbitals of the Eu atoms. The Coulomb repulsion within these orbitals promotes an antiferromagnetic alignment of the magnetic moments, resulting in cancellation of the net magnetic moment within the cell. In the resulting AFM-Néel state, we calculated the magnitude of the magnetic moments on the magnetic Eu atoms as $6.07 \mu_B$. However, to simplify further magnetic calculations in Monte Carlo simulations, we rounded this value to $6.00 \mu_B$. This rounded value still captures the essential magnetic behavior of the system and ensures computational efficiency in subsequent simulations. These findings demonstrate the significant influence of both spin-orbit coupling and electron-electron interactions on the magnetic ground state of the EuCl_3 monolayer. The transition from ferromagnetic to antiferromagnetic behavior highlights the delicate balance between competing magnetic interactions in this system, which can be harnessed for potential applications in spintronics and magnetic devices.

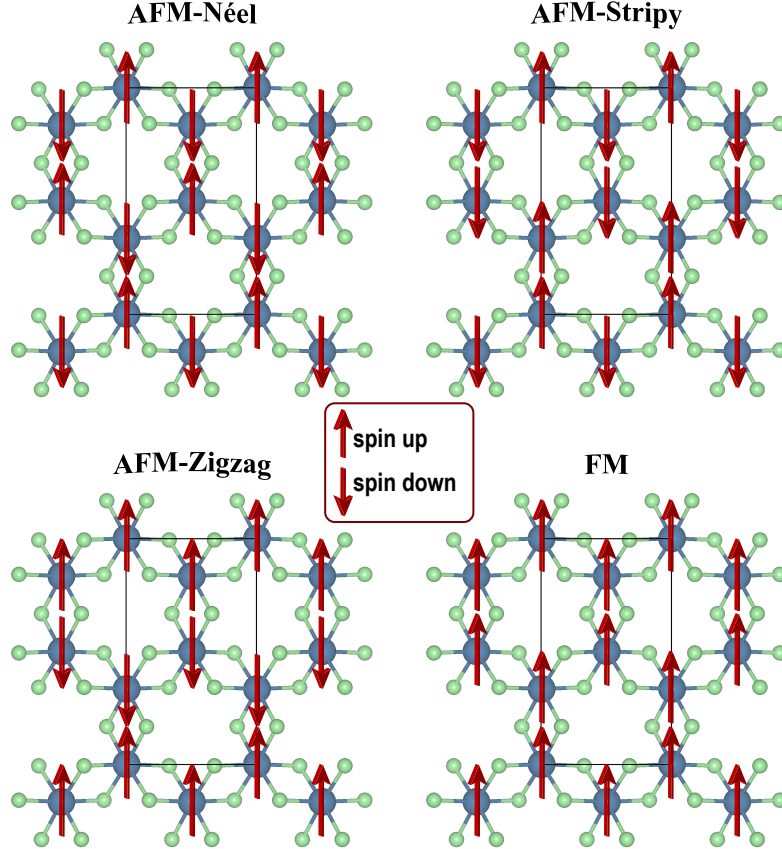


Figure 2. Magnetic configurations investigated for the EuCl_3 monolayer. Arrows pointing upwards indicate spin-up states, while arrows pointing downwards represent spin-down states.

In the AFM-Néel ground state of the EuCl_3 monolayer, we first examined the stability of its atomic structure. The monolayer exhibits a cohesive energy of 3.50 eV per atom, which indicates a strong binding between the atoms. To further assess its stability, we conducted dynamical stability analyses through phonon calculation, without taking into account the effects of SOC due to its computational cost. In the Supporting Information⁴⁹, we presented our findings regarding the phonon frequencies throughout the Brillouin zone, as well as the phonon projected density of states. Remarkably, we observed predominantly positive phonon frequencies throughout the entire Brillouin zone, with the exception of the region around the Y -point. However, it is important to note that despite the negativity observed around the Y -point, our analysis reveals that there is no density of states below the zero frequency level. This indicates that the EuCl_3 monolayer exhibits overall stability and is not prone to instability.

After achieving its stable ground state in the AFM-Néel configuration, we conducted a comprehensive investigation of the electronic properties of the EuCl_3 monolayer. To explore the electronic charge transfer mechanism within the system, we employed Bader charge analysis⁵⁴. Our calculations demonstrated that each Eu atom donated $2.01 e$, resulting in a cumulative transfer of 8.04 electrons that were equally shared among the Cl atoms. As a consequence,

each Cl atom exhibited an excess charge of 0.67 e. Further information regarding this charge transfer mechanism, the calculated charge density difference isosurfaces, can be found in the Supporting Information⁴⁹. These isosurfaces were obtained by subtracting the charge densities of isolated atoms from the entire system's charge density. The observed direction of charge transfer aligns with the concept of Pauling electronegativity, indicating that the electronegative Cl atoms tend to gain electrons while the Eu atoms, being less electronegative, donate electrons. For Cl, the Pauling electronegativity is known to be 3.12, whereas there are no reliable sources for Eu other than the one reported by Pauling in 1960⁵⁵ with the value falling within the range of 1.1-1.2. Besides, we determined the work function of the AFM-Néel EuCl₃ monolayer by using the Equation 1. The work function, a fundamental concept in solid-state physics, represents the minimum thermodynamic work (i.e., energy) required to extract an electron from a solid to a point in the vacuum located immediately outside the solid surface. Our calculations yielded a work function of $W=0.57$ eV for the AFM-Néel EuCl₃ monolayer. Furthermore, we performed electronic energy band structure calculations for the EuCl₃ monolayer, in the AFM-Néel ground state, using both the standard PBE functional and the HSE hybrid functional, which is known for its improved accuracy in predicting band gap values. Additionally, we generated the corresponding total and partial electronic density of states (PDOS) graphs through PBE functional. All these plots have been presented in the Supporting Information⁴⁹. Our investigation of the electronic energy band diagrams under the PBE functional, calculated along the major symmetry directions of the Brillouin zone, demonstrates a semiconductor behavior with a band gap value of 1.75 eV. However, the HSE functional predicts the EuCl₃ monolayer to be an insulator, featuring a significantly wider band gap of 4.99 eV. Analyzing the partial DOS graph in detail, we observed that the main contribution to the valence bands around the Fermi level originates from Cl atoms, with a relatively minor contribution from Eu atoms. Furthermore, we found that the DOS of Eu atoms in the valence bands is primarily due to *d*-orbital electrons, while *f*-orbital DOSs remain nearly negligible. In contrast, the conduction bands feature a rather flat band around 1.60 eV, predominantly arising from the *f*-orbitals of Eu atoms. The presence of *f*-orbital electrons in the conduction band indicates a significant role of Eu's 4*f* electronic states in the conducting behavior of the EuCl₃ monolayer.

Next, we focused on investigating the magnetic properties of the EuCl₃ monolayer, which constituted the primary objective of our research. To accomplish this, we employed an atomistic spin Hamiltonian based on a classical Heisenberg model, represented by Equation 2. By utilizing this model, we calculated the magnetic exchange coupling parameters, denoted as J_1 , J_2 , and J_3 , which are essential components of the aforementioned equation. Our calculations yielded the following values for these parameters: $J_1=-0.307$ meV, $J_2=-0.099$ meV, and $J_3=-0.405$ meV. These values represent the strengths of the magnetic interactions within the EuCl₃ monolayer. Additionally, we determined the magnetic anisotropy energies (MAEs) of the monolayer, both in-plane ($E[100] - E[010]$) and out-of-plane ($E[100] - E[001]$). The calculated values for the in-plane and out-of-plane MAEs were found to be 479 meV and 573 meV, respectively. These values of magnetic anisotropy constants indicate that the major contribution to the total order parameter comes from the *z*-component of magnetic dipole moment.

Fig. 3 illustrates the temperature-dependent behavior of the order parameter \mathbf{O} and heat capacity \mathbf{C} of the EuCl₃ monolayer. The Néel order parameter $\mathbf{O}(T)$, representing the staggered magnetization, displays a distinct variation. The curve reveals that the ground state of the system is characterized by an antiferromagnetic (AFM) arrangement. As the temperature T increases toward the critical region, a magnetic order emerges, and the order parameter reaches saturation at a value of $\mu \approx 6.0$ within a sufficiently low-temperature regime. To identify the critical temperature of the system, we examine the variation of the heat capacity, represented by the curve \mathbf{C} vs. T . The temperature corresponding to the peak position in this curve is recognized as the critical temperature. Our analysis indicates that the critical temperature, denoted as T_N , is determined to be 390 K. This finding demonstrates that the magnetic order in the EuCl₃ monolayer can be sustained above room temperature.

IV. CONCLUSION

In this study, we have thoroughly investigated the structural, electronic, and magnetic properties of the EuCl₃ monolayer, focusing on its potential applications in spintronics and magnetic devices. We found that the monolayer adopts a trigonal symmetry within the $P\bar{3}1m$ space group, with europium (Eu) atoms forming an octahedral coordination geometry coordinated by six chlorine (Cl) atoms. The ground state of the EuCl₃ monolayer exhibits a delicate balance between competing magnetic interactions, transitioning from a ferromagnetic to an antiferromagnetic Néel state when incorporating spin-orbit coupling (SOC) and electron-electron interactions through the PBE+SOC+U calculation. Regarding the electronic properties, our investigations showed that the EuCl₃ monolayer exhibited a semiconductor behavior with a band gap of 1.75 eV under the PBE functional and a significantly wider band gap of 4.99 eV when calculated with the HSE hybrid functional. The conducting behavior was found to be influenced by the 4*f* electronic states of the Eu atoms. Finally, through the temperature-dependent behavior of the order parameter and heat capacity, we found that the EuCl₃ monolayer exhibited an antiferromagnetic ground state with a critical

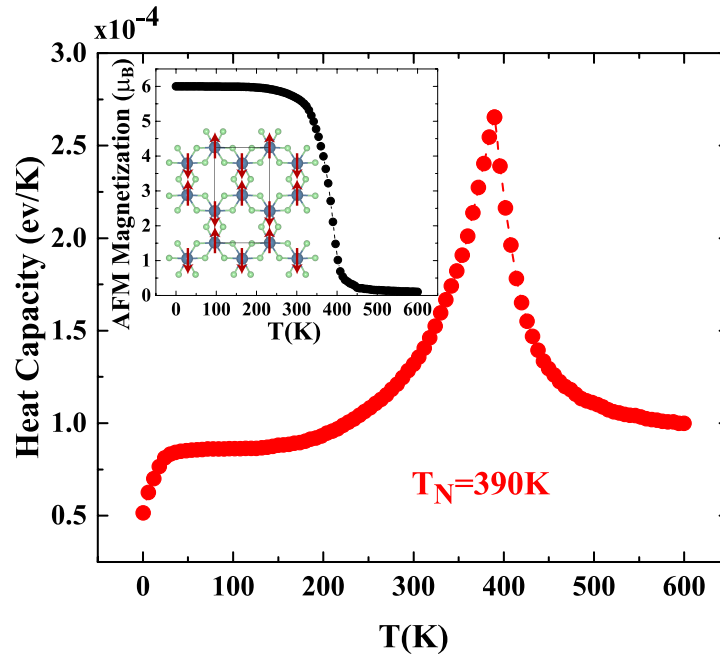


Figure 3. Variation of the heat capacity C as a function of temperature T . The inset shows the temperature dependence of AFM Néel magnetization and the schematic diagram depicts the ground state magnetic configuration of Eu atoms.

temperature of 390 K, indicating the potential for maintaining magnetic order above room temperature.

ACKNOWLEDGMENTS

The computational resources are provided by TÜBİTAK ULAKBİM, High Performance and Grid Computing Center (TR-Grid e-Infrastructure), and the Leibniz Supercomputing Centre. E. A. acknowledges the Alexander von Humboldt Foundation for a Research Fellowship for Experienced Researchers. IO thanks to the Council of Higher Education (the CoHE) 100/2000 Program and to the Scientific and Technological Research Council of Turkey (TUBITAK) BİDEB-2214/A Program for providing doctoral scholarships. This research was supported by Aydin Adnan Menderes University Research Fund (Project Number: FEF-21032).

* ethem.akturk@adu.edu.tr

- ¹ W. Zhang, P. K. J. Wong, R. Zhu, and A. T. Wee, *InfoMat* **1**, 479 (2019).
- ² D. R. Klein, D. MacNeill, J. L. Lado, D. Soriano, E. Navarro-Moratalla, K. Watanabe, T. Taniguchi, S. Manni, P. Canfield, J. Fernández-Rossier, and P. Jarillo-Herrero, *Science* **360**, 1218 (2018).
- ³ Y. Khan, S. M. Obaidulla, M. R. Habib, A. Gayen, T. Liang, X. Wang, and M. Xu, *Nano Today* **34**, 100902 (2020).
- ⁴ X. Wang, J. Tang, X. Xia, C. He, J. Zhang, Y. Liu, C. Wan, C. Fang, C. Guo, W. Yang, Y. Guang, X. Zhang, H. Xu, J. Wei, M. Liao, X. Lu, J. Feng, X. Li, Y. Peng, H. Wei, R. Yang, D. Shi, X. Zhang, Z. Han, Z. Zhang, G. Zhang, G. Yu, and X. Han, *Science Advances* **5**, eaaw8904 (2019).
- ⁵ Y. Feng, X. Wu, L. Hu, and G. Gao, *Journal of Materials Chemistry C* **8**, 14353 (2020).
- ⁶ L. Webster and J.-A. Yan, *Physical Review B* **98**, 144411 (2018).
- ⁷ H. Li, S. Ruan, and Y.-J. Zeng, *Advanced Materials* **31**, 1900065 (2019).
- ⁸ D. L. Cortie, G. L. Causer, K. C. Rule, H. Fritzsche, W. Kreuzpaintner, and F. Klose, *Advanced Functional Materials* **30**, 1901414 (2020).
- ⁹ N. D. Mermin and H. Wagner, *Physical Review Letters* **17**, 1133 (1966).
- ¹⁰ B. Huang, G. Clark, E. Navarro-Moratalla, D. R. Klein, R. Cheng, K. L. Seyler, D. Zhong, E. Schmidgall, M. A. McGuire, D. H. Cobden, *et al.*, *Nature* **546**, 270 (2017).
- ¹¹ J. L. Lado and J. Fernández-Rossier, *2D Materials* **4**, 035002 (2017).
- ¹² C. Xu, J. Feng, H. Xiang, and L. Bellaiche, *npj Computational Materials* **4**, 57 (2018).

- ¹³ M. Gibertini, M. Koperski, A. F. Morpurgo, and K. S. Novoselov, *Nature Nanotechnology* **14**, 408 (2019).
- ¹⁴ C. Gong, L. Li, Z. Li, H. Ji, A. Stern, Y. Xia, T. Cao, W. Bao, C. Wang, Y. Wang, Z. Q. Qiu, R. J. Cava, S. G. Louie, J. Xia, and X. Zhang, *Nature* **546**, 265 (2017).
- ¹⁵ Y. Deng, Y. Yu, Y. Song, J. Zhang, N. Z. Wang, Z. Sun, Y. Yi, Y. Z. Wu, S. Wu, J. Zhu, J. Wang, X. H. Chen, and Y. Zhang, *Nature* **563**, 94 (2018).
- ¹⁶ M. Bonilla, S. Kolekar, Y. Ma, H. C. Diaz, V. Kalappattil, R. Das, T. Eggers, H. R. Gutierrez, M.-H. Phan, and M. Batzill, *Nature Nanotechnology* **13**, 289 (2018).
- ¹⁷ C. Gong and X. Zhang, *Science* **363**, eaav4450 (2019).
- ¹⁸ M. Kim, P. Kumaravadeivel, J. Birkbeck, W. Kuang, S. G. Xu, D. Hopkinson, J. Knolle, P. A. McClarty, A. Berdyugin, M. Ben Shalom, R. V. Gorbachev, S. J. Haigh, S. Liu, J. H. Edgar, K. S. Novoselov, I. V. Grigorieva, and A. K. Geim, *Nature Electronics* **2**, 457 (2019).
- ¹⁹ C. Bacaksiz, D. Šabani, R. Menezes, and M. Milošević, *Physical Review B* **103**, 125418 (2021).
- ²⁰ D. R. Klein, D. MacNeill, Q. Song, D. T. Larson, S. Fang, M. Xu, R. A. Ribeiro, P. C. Canfield, E. Kaxiras, R. Comin, and P. Jarillo-Herrero, *Nature Physics* **15**, 1255 (2019).
- ²¹ M. Serri, G. Cucinotta, L. Poggini, G. Serrano, P. Sainctavit, J. Strychalska-Nowak, A. Politano, F. Bonaccorso, A. Caneschi, R. J. Cava, R. Sessoli, L. Ottaviano, T. Klimczuk, V. Pellegrini, and M. Mannini, *Advanced Materials* **32**, 2000566 (2020).
- ²² A. M. Tokmachev, D. V. Averyanov, A. N. Taldenkov, O. E. Parfenov, I. A. Karateev, I. S. Sokolov, and V. G. Storchak, *Materials Horizons* **6**, 1488 (2019).
- ²³ X. Jiang, Q. Liu, J. Xing, N. Liu, Y. Guo, Z. Liu, and J. Zhao, *Applied Physics Reviews* **8**, 031305 (2021).
- ²⁴ J. Law, R. V. Ramanujan, and V. Franco, *Journal of Alloys and Compounds* **508**, 14 (2010).
- ²⁵ J. Shen, J.-F. Wu, and J.-R. Sun, *Journal of Applied Physics* **106**, 083902 (2009).
- ²⁶ V. Percharsky and K. Gschneidner Jr, *Physical Review Letters* **78**, 4494 (1997).
- ²⁷ M. H. N. Assadi, J. J. G. Moreno, D. A. Hanaor, and H. Katayama-Yoshida, *Physical Chemistry Chemical Physics* **23**, 20129 (2021).
- ²⁸ P. Chakraborty, S. Dey, and S. Basu, *Physica B: Condensed Matter* **601**, 412677 (2021).
- ²⁹ R. Zhao, P. Wang, T. Yang, Z. Li, B. Xiao, and M. Zhang, *The Journal of Physical Chemistry C* **119**, 28679 (2015).
- ³⁰ A. Franco Jr, H. Pessoni, and M. Soares, *Journal of Magnetism and Magnetic Materials* **355**, 325 (2014).
- ³¹ A. Masago, H. Shinya, T. Fukushima, K. Sato, and H. Katayama-Yoshida, *AIP Advances* **10**, 025216 (2020).
- ³² M. A. Kishore, H. Okamoto, L. Patra, R. Vidya, A. O. Sjästad, H. Fjellvåg, and P. Ravindran, *Physical Chemistry Chemical Physics* **18**, 27885 (2016).
- ³³ A. P. Durajski, A. E. Auguscik, and R. Szczyński, *Physica E: Low-dimensional Systems and Nanostructures* **119**, 113985 (2020).
- ³⁴ N. E. Kirchner-Hall, W. Zhao, Y. Xiong, I. Timrov, and I. Dabo, *Applied Sciences* **11**, 2395 (2021).
- ³⁵ S. Das, M. Bhuyan, and M. Basith, *Journal of Materials Research and Technology* **13**, 2408 (2021).
- ³⁶ F. Ersan, E. Vatansever, S. Sarikurt, Y. Yüksel, Y. Kadioglu, H. D. Ozaydin, O. Ü. Aktürk, Ü. Akıncı, and E. Aktürk, *Journal of Magnetism and Magnetic Materials* **476**, 111 (2019).
- ³⁷ Y. Z. Abdullahi, S. Ahmad, and A. A. Ibrahim, *RSC Advances* **11**, 35061 (2021).
- ³⁸ G. Kresse and J. Furthmüller, *Computational Materials Science* **6**, 15 (1996).
- ³⁹ G. Kresse and J. Furthmüller, *Physical Review B* **54**, 11169 (1996).
- ⁴⁰ P. E. Blöchl, *Physical Review B* **50**, 17953 (1994).
- ⁴¹ G. Kresse and D. Joubert, *Physical Review B* **59**, 1758 (1999).
- ⁴² J. P. Perdew, K. Burke, and M. Ernzerhof, *Physical Review Letters* **77**, 3865 (1996).
- ⁴³ S. Grimme, *Journal of Computational Chemistry* **27**, 1787 (2006).
- ⁴⁴ H. J. Monkhorst and J. D. Pack, *Physical Review B* **13**, 5188 (1976).
- ⁴⁵ C. G. Broyden, *IMA Journal of Applied Mathematics* **6**, 76 (1970).
- ⁴⁶ C. G. Broyden, *IMA Journal of Applied Mathematics* **6**, 222 (1970).
- ⁴⁷ K. Momma and F. Izumi, *Journal of Applied Crystallography* **44**, 1272 (2011).
- ⁴⁸ M. Cococcioni and S. De Gironcoli, *Physical Review B* **71**, 035105 (2005).
- ⁴⁹ See Electronic Supplementary Information (ESI) at [URL will be inserted by publisher] for ...
- ⁵⁰ R. Pradip, P. Piekarz, A. Bosak, D. Merkel, O. Waller, A. Seiler, A. Chumakov, R. Rüffer, A. Oleś, K. Parlinski, *et al.*, *Physical Review Letters* **116**, 185501 (2016).
- ⁵¹ C. Kittel and P. McEuen, *Introduction to solid state physics* (John Wiley & Sons, 2018).
- ⁵² M. E. Newman and G. T. Barkema, *Monte Carlo methods in statistical physics* (Clarendon Press, 1999).
- ⁵³ D. Landau and K. Binder, *A guide to Monte Carlo simulations in statistical physics* (Cambridge University Press, 2021).
- ⁵⁴ G. Henkelman, A. Arnaldsson, and H. Jónsson, *Computational Materials Science* **36**, 354 (2006).
- ⁵⁵ L. Pauling, Ithaca, New York (1960).